frontiers | Frontiers in Materials

TYPE Original Research
PUBLISHED 07 September 2023
DOI 10.3389/fmats.2023.1267961

Check for updates

OPEN ACCESS

EDITED BY
Yu-Fei Wu,
RMIT University, Australia

REVIEWED BY
Angelo Aloisio,
University of L'Aquila, Italy
Jun He,
Changsha University of Science and Technology, China

*CORRESPONDENCE
Liangqin Jiang,
jiangliangqin1978@163.com
Jing Ji,
jijing1977@163.com

RECEIVED 27 July 2023
ACCEPTED 22 August 2023
PUBLISHED 07 September 2023

CITATION
He J, Jiang L, Ji J, Zhang Z, Chu X, Hong Y and Zhang H (2023), Seismic behavior of steel-reinforced high-strength concrete composite beams with bonded tendons. *Front. Mater.* 10:1267961. doi: 10.3389/fmats.2023.1267961

COPYRIGHT
© 2023 He, Jiang, Ji, Zhang, Chu, Hong and Zhang. This is an open-access article distributed under the terms of the Creative Commons Attribution License (CC BY). The use, distribution or reproduction in other forums is permitted, provided the original author(s) and the copyright owner(s) are credited and that the original publication in this journal is cited, in accordance with accepted academic practice. No use, distribution or reproduction is permitted which does not comply with these terms.

Seismic behavior of steel-reinforced high-strength concrete composite beams with bonded tendons

Jinjin He[1], Liangqin Jiang[1]*, Jing Ji[1,2]*, Zhanbin Zhang[1], Xuan Chu[1], Yigang Hong[1] and Huiling Zhang[1]

[1]Heilongjiang Key Laboratory of Disaster Prevention Mitigation and Protection Engineering, Northeast Petroleum University, Daqing, China, [2]China-Pakistan Belt and Road Joint Laboratory on Smart Disaster Prevention of Major Infrastructures, Southeast University, Nanjing, China

To study the seismic behavior of steel-reinforced high-strength concrete composite beams with bonded tendons (PSRHSCBs) under low cyclic loading, 13 PSRHSCBs were designed with the main parameters of the span-to-height ratio of beams (L/H), the cubic strength of concrete (fcu), the eccentricity of H-shaped steel (eH), the volume stirrup ratio (pv), the longitudinal reinforcement ratio (p), and the tension control stress of tendons(σcon). Using the simplified bilinear constitutive model of steel and the nonlinear constitutive model of high-strength concrete, and introducing plastic damage of concrete, fine finite element models were established with ABAQUS software. 11 similar test specimens were conducted by above modeling method, by comparing existing test curves and numerical simulation curves, both of them match well, which verified the validity of the modeling method. Subsequently, parameter analysis for 13 PSRHSCB specimens was performed, and the influence regularity of different parameters on the seismic behavior of this kind of composite beams was obtained. The results show that hysteretic curves of this kind of composite beams are full, and the failure mode is manifested as bending failure. The ultimate load, the energy dissipation capacity and the ductility coefficient of specimens can be improved significantly by increasing pv, on the contrary, the energy dissipation capacity and the ductility coefficient decrease gradually by increasing fcu. The stiffness degradation of specimens significantly slows down with the increasing of L/H and σcon, and the decreasing of eH. Finally, the trilinear skeleton curve model and the restoring force model are established by statistical regression, and the corresponding seismic design suggestions are given, and these can provide theoretical support for the seismic design of such composite beams in actual engineering.

KEYWORDS

steel-reinforced high-strength concrete beams, prestressing tendons, finite element model, seismic behavior, restoring force model

1 Introduction

With the advancement of construction engineering towards the super high, heavy load and large span, the traditional reinforced concrete beams' limitations applied to large-span structures are becoming more and more prominent. To solve this problem, the research group has proposed the assembled prestressed steel-reinforced high-strength concrete composite frame structure system (Ji et al., 2023a), which utilizes fully prestressed steel-

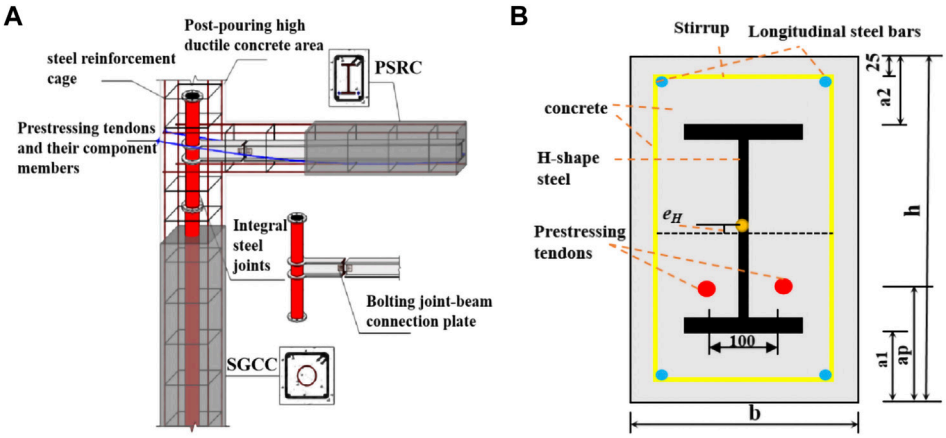

FIGURE 1
(A) The schematic diagram of new assembled frame; **(B)** The sectional arrangements of this kind of composite beams.

reinforced concrete beams (PSRCB) to achieve larger spans, as shown in Figure 1A. By incorporating prestressing tendons within steel-reinforced concrete beams and applying prestress to them, the flexural stiffness of composite beams during normal use can be improved significantly, and the crack resistance of the composite beams can also be enhanced greatly (Sun et al., 2006; Wang et al., 2009; Zhou et al., 2009; Xue et al., 2007). High-strength concrete (HSC) has the characteristics of high strength and good durability. The application of HSC in PSRCB can improve the bearing capacity and stiffness of composite beams significantly, and reduce the sectional size of beams, and improve the service life of beam members in long-span, heavy load, corrosion, and earthquake environments in further (Ahmad and Shah, 1985; Graybeal, 2008; Steninberg, 2010; Taylor et al., 2011), so the steel-reinforced high-strength concrete beams with bonded tendons (PSRHSCB) are more suitable for long-span, heavy-load, super high-rise buildings (Yao et al., 2014; Kuntal et al., 2017; Wang et al., 2018), and it is of a very broad application prospect for this kind of PSRHSCBs in actual engineering.

In recent years, there has been extensive research at home and abroad on the mechanical properties of PSRHSCBs (Akiyama et al., 2012; Wu et al., 2019; Jiang et al., 2021). Ji et al. (Ji et al., 2011) carried out simulations and analyses on seven PSRCBs, and the influence regularity of various parameters on the monotonic bending moment-curvature curves of the section and the monotonic load-displacement curves of the components was obtained, finally, the ductility formula and restoring force model for this kind of beams were established systematically by statistical regression. Wang et al. (Wang et al., 2009) employed ANSYS to simulate the bending process of 10 PSRHSCBs under static loads, and by comparisons with experimental data, the results revealed that the cracking load, ultimate load, yield load of the steel bars, and the load-displacement curves obtained from simulation closely matched the experimental results. This confirmation provides strong evidence for the accuracy of the finite element model. In another study, Jia et al. (2013a) conducted shear capacity tests on 8 PSRHSCBs, and the normal section cracking load, yield load, failure mode, and ultimate shear capacity subjected to concentrated loads were examined, and the impacts of various parameters on the shear capacity and ductility of the beams were analyzed. Through regression analysis, the calculation formula for the shear capacity of this kind of beams was proposed. Based on these findings, Jia et al. (2013b) further investigated the shear mechanism of PSRHSCBs by conducting shear performance tests on 14 PSRHSCB specimens and 7 prestressed ultra-high-strength concrete beam (PSRUHSCB) specimens. According to the load-mid-span deflection curves obtained from the test, the influence of different test parameters on the shear ductility of the test beams was studied, and the shear capacity formula of PSRUHSCBs was proposed. Meng et al. (Meng et al., 2014) carried out bending test of 13 PSRUHSCBs and systematically analyzed the failure mode, crack development, and distribution law of the specimens. The relationship between the load level and the comprehensive reinforcement index was investigated, and the formulas for calculating the average crack distance and maximum crack width were put forward. Lu et al. (2021) conducted bending test of 4 partially PSRUHSCBs and one partially prestressed ultra-high strength concrete beams under fatigue load. The load-deflection curves and the correlation between the tensile strain of the non-prestressed tensile steel bar as well as the regulation for degradation of the bending stiffness were obtained, and the results showed that the equivalent stress level was the main factor for the fatigue failure of the specimens. In summary, scholars at home and abroad have carried out a large number of experimental studies on the shear and flexural behavior of PSRHSCBs under static loads, but there are few reports on the seismic behavior of PSRHSCBs under low cyclic loading.

Therefore, to deeply investigate the seismic behavior of PSRHSCBs, 13 PSRHSCBs are designed with the main parameters of the span-to-height ratio of beams (L/H), the cubic strength of concrete (f_{cu}), the eccentricity of H-shaped steel (e_H), the volume stirrup ratio (p_v), the longitudinal reinforcement ratio (p), and the tension control stress of tendons(σ_{con}) in this paper. ABAQUS software is used to carry out the simulation analysis under low cyclic loading, and hysteretic curves and failure modes

TABLE 1 The main parameters of 13 PSRHSCB specimens.

Specimens	$h \times b$ (mm×mm)	a_1 (mm)	a_2 (mm)	a_p (mm)	f_{cu} (Mpa)	L/H	p_v (%)	e_H (mm)	p (%)	σ_{con}	$S_\triangle$	
											Up	Down
PSRHSCB-1	320 × 220	60	60	105	60	9.375	0.66	0	1.7	$0.7f_{ptk}$	2Φ18	2Φ18
PSRHSCB-2	360 × 220	80	80	125	60	8.300	0.66	0	1.5	$0.7f_{ptk}$	2Φ18	2Φ18
PSRHSCB-3	400 × 220	100	100	145	60	7.500	0.66	0	1.3	$0.7f_{ptk}$	2Φ18	2Φ18
PSRHSCB-4	320 × 220	60	60	105	70	9.375	0.66	0	1.3	$0.7f_{ptk}$	2Φ18	2Φ18
PSRHSCB-5	320 × 220	60	60	105	80	9.375	0.66	0	1.3	$0.7f_{ptk}$	2Φ18	2Φ18
PSRHSCB-6	320 × 220	60	60	105	60	9.375	0.55	0	1.3	$0.7f_{ptk}$	2Φ18	2Φ18
PSRHSCB-7	320 × 220	60	60	105	60	9.375	0.44	0	1.3	$0.7f_{ptk}$	2Φ18	2Φ18
PSRHSCB-8	400 × 220	80	120	125	60	7.500	0.62	20	1.3	$0.7f_{ptk}$	2Φ18	2Φ18
PSRHSCB-9	400 × 220	60	140	105	60	7.500	0.62	40	1.3	$0.7f_{ptk}$	2Φ18	2Φ18
PSRHSCB-10	400 × 220	60	140	105	60	7.500	0.62	40	1.6	$0.7f_{ptk}$	3Φ18	2Φ18
PSRHSCB-11	400 × 220	60	140	105	60	7.500	0.62	40	1.9	$0.7f_{ptk}$	4Φ18	2Φ18
PSRHSCB-12	320 × 220	60	60	105	60	9.375	0.66	0	1.3	$0.6f_{ptk}$	2Φ18	2Φ18
PSRHSCB-13	320 × 220	60	60	105	60	9.375	0.66	0	1.3	$0.8f_{ptk}$	2Φ18	2Φ18

are gotten, then the load-displacement (P-Δ) skeleton curves of this kind of beams are extracted. The influence regularity of different parameters on the seismic behavior of such beams are obtained. Based on the parameter study, the trilinear model of PSRHSCBs skeleton curve and the restoring force model of PSRHSCBs are established by statistical regression, and the corresponding seismic design suggestions are given, and these can provide theoretical support for the application and promotion of this kind of beams in practical engineering.

2 Specimens design

To investigate the seismic behavior of PSRHSCBs under low cyclic loading, A total of 13 PSRHSCB specimens are designed with the main parameters of the span-to-height ratio (L/H) of the beams, the cubic strength of concrete (f_{cu}), the eccentricity of H-shaped steel (e_H), the volume stirrup ratio (p_v), the longitudinal reinforcement ratio (p), and the tension control stress (σ_{con}), as shown Table 1. All specimens own with a span (L) of 3,000 mm, and the cross-sectional sizes ($h \times b$) of specimens include 320 mm × 220 mm, 360 mm × 220 mm, and 400 mm × 220 mm, so the span-to-height ratios (L/H) of specimens are 9.375, 8.300, and 7.500, respectively. The cubic strength of concrete (f_{cu}) is 60, 70 and 80 Mpa, respectively. The Q235 H-shaped steels are adopted with a cross-sectional size of HN200 × 100 × 5.5 × 8. The H-shaped steels are arranged in three configurations: central symmetry, the eccentricity of 20 mm downward, and eccentricity of 40 mm downward. HRB335 steel bars with a diameter of 18 mm are used as longitudinal reinforcement within the beams. HPB235 steel bars with a diameter of 8 mm are used as the stirrups. Additionally, two 1860 Mpa (f_{ptk}) high-efficiency low-relaxation steel strands with a diameter of 15.2 mm are used for prestressing tendons. These prestressing tendons are symmetrically arranged on both sides of the H-shaped steel. The tension control stresses (σ_{con}) is 0.6 f_{ptk}, 0.7 f_{ptk}, and 0.8 f_{ptk}, respectively. The cross-sectional arrangements of the specimens are shown in Figure 1B.

3 Finite element model

3.1 Constitutive model for materials

3.1.1 Steel

Based on the Mises yield criterion (Aleksandrova et al., 2012), the ideal elastic-plastic constitutive model (CM) (Ji et al., 2023b) is adopted for the CMs of H-shape steels, longitudinal steel bars, and stirrups as shown in Figure 2A. The expression of the CM can be seen in Eq. 1. The mechanical properties of three kinds of steels are listed in Table 2.

$$\sigma = \begin{cases} E_s\varepsilon, \varepsilon \le \varepsilon_{yk} \\ f_{yk}, \varepsilon > \varepsilon_{yk} \end{cases} \tag{1}$$

Where, E_s is the elastic modulus of steel, and f_{yk} is the yield strength of steel, and ε_{yk} is the strain at the yield strength.

3.1.2 Prestressing tendons

The expression of the CM for prestressing tendons can be seen in Eq. 2. The mechanical properties of prestressing tendon are shown in Table 2. The CM of prestressing tendons is shown in Figure 2B.

$$\sigma = \begin{cases} E_P\varepsilon_P, \varepsilon_P \le \varepsilon_{Py} \\ f_{Py} + k\left(\varepsilon_{Py} - \varepsilon_y\right), \varepsilon_{Py} < \varepsilon_P < \varepsilon_{pu} \\ 0, \varepsilon > \varepsilon_{yk} \end{cases} \tag{2}$$

Where, σ is the stress of prestressing tendon, E_p is the elastic modulus of prestressing tendon, f_{py} is the nominal yield strength of

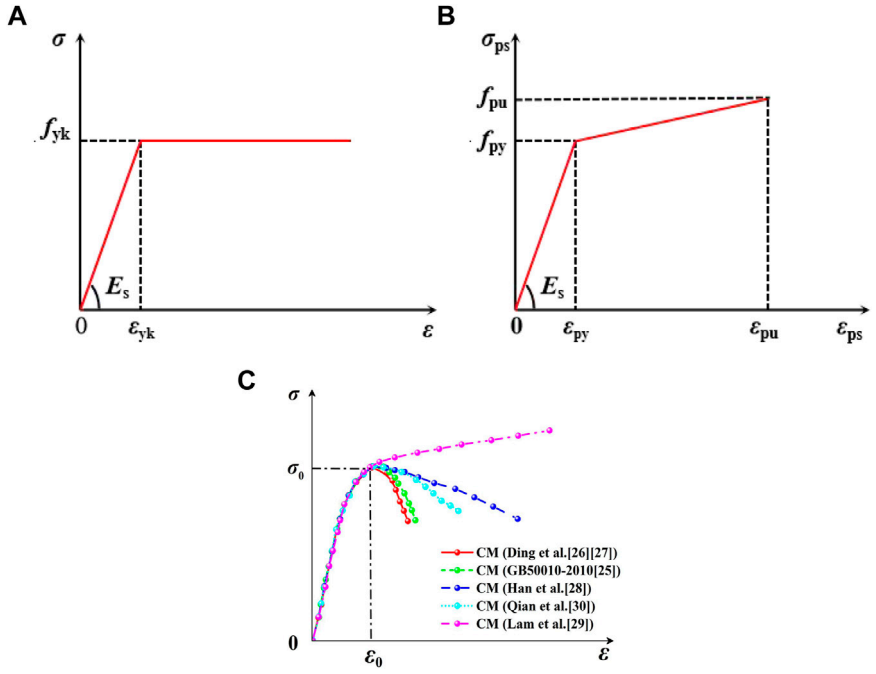

FIGURE 2
(A) The constitutive model of steel; **(B)** The constitutive model of prestressing tendon; **(C)** The constitutive model of concrete.

TABLE 2 The mechanical properties of three kinds of steels and prestressing tendons.

Material type	Strength grade	Yield strength f_y/Mpa	Tensile strength f_u/Mpa	Elastic modulus E/Mpa
H-shape steels	Q235	235	370	2.1×10^5
Longitudinal steel bars	HRB400	335	455	2.0×10^5
Stirrups	HPB235	235	370	2.1×10^5
Prestressing tendons	1860	-	1860	1.95×10^5

prestressing tendon, f_{pu} is the ultimate strength of prestressing tendon, ε_p is the strain of prestressing tendon, ε_{py} is the nominal yield strain of prestressing tendon, ε_{pu} is the ultimate strain of prestressing tendon, and k is the slope of a hardened section of the prestressing tendon, $k = \frac{(f_{pu}-f_{py})}{(\varepsilon_{pu}-\varepsilon_{py})}$.

Where, ε_{pu} is equal to 0.035 (PARK, 1989), $f_{py} = 0.75f_{pu}$, $E_p = 1.95 \times 10^5 \mathrm{N/mm^2}$, $\varepsilon_{py} = f_{py}/E_p$.

3.1.3 Concrete

1. The comparisons of CMs for concrete proposed by Qian et al., (2002), Teng et al., (2003), Han et al., (2001), Yu and Ding, (2003); (Ding and Yu, 2004) and the Code for Design of Concrete Structure (GB50010-2010) (Zhao et al., 2015) are shown in Figure 2C. When the strength levels of concrete are less than C60, the unconstrained concrete constitutive model proposed in the GB50010-2010 (Zhao et al., 2015) is used.

(1) Calculation formula for the stress-strain relationship of concrete under uniaxial tension is shown in Eq. 3.

$$\sigma = (1 - d_t)E_c\varepsilon \tag{3}$$

$$d_t \begin{cases} 1 - \rho_t[1.2 - 0.2x^5], x \le 1 \\ 1 - \dfrac{\rho_t}{\alpha_t(x-1)^{1.7} + x}, x > 1 \end{cases} \tag{4}$$

Where $x = \varepsilon/\varepsilon_{t,r}$, $\rho_t = f_{t,r}/E_c\varepsilon_{t,r}$. The specific physical meaning of variables is given in reference (Zhao et al., 2015).

(2) Calculation formula for the stress-strain relationship of concrete under uniaxial compression is shown in Eq. 5.

$$\sigma = (1 - d_c)E_c\varepsilon \tag{5}$$

$$d_c \begin{cases} 1 - \dfrac{\rho_c n}{n - 1 + x^n}, x \le 1 \\ 1 - \dfrac{\rho_c}{\alpha_c(x-1)^2 + x}, x > 1 \end{cases} \tag{6}$$

Where, $x = \varepsilon/\varepsilon_{c,r}$, $n = E_c\varepsilon_{c,r}/(E_c\varepsilon_{c,r} - f_{c,r})$. The specific physical meaning of variables is given in reference (Zhao et al., 2015).

2. When the strength levels of concrete are greater than or equal to C60, the stress-strain relationship of concrete proposed by Yu and Ding (Yu and Ding, 2003; Ding and Yu, 2004) is adopted, which is simple in form and has good calculation accuracy.

TABLE 3 The parameters of concrete plastic damage model.

Dilation angle (°)	Eccentricity	f_{bo}/f_{co}	K	Viscosity parameter
38	0.1	1.16	0.667	0.0005

Note: K is the invariant stress ratio. f_{bo}/f_{co} is the ultimate strength ratio of biaxial compression to uniaxial compression.

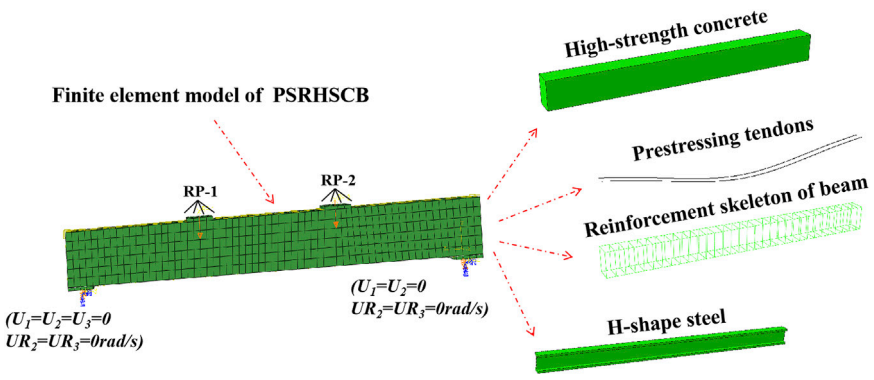

FIGURE 3
Finite element model of PSRHSCB.

(1) Equation of the stress-strain relationship curve for concrete under tension is shown in Eq. 7.

$$y = \begin{cases} \dfrac{Ax - x^2}{1 + (A-2)x}, x \le 1 \\ \dfrac{x}{\alpha(x-1)^{1.7} + x}, x > 1 \end{cases} \tag{7}$$

Where, $y = \sigma/f_t$, $x = \varepsilon/\varepsilon_{tp}$, $A = 1.306$, $\alpha = 1 + 0.025 f_t^3$, and other variables can be found in reference (Ding and Yu, 2004).

(2) Equation of the stress-strain relationship curve for concrete compressive strength is shown in Eq. 8.

$$y = \begin{cases} \dfrac{A_1 x - x^2}{1 + (A_1 - 2)x}, x \le 1 \\ \dfrac{x}{\alpha_1 (x-1)^2 + x}, x > 1 \end{cases} \tag{8}$$

Where, $y = \sigma/f_c$, $x = \varepsilon/\varepsilon_0$, $A_1 = 9.1 f_{cu}^{-4/9}$, $\alpha_1 = 2.5 \times 10^{-5} f_{cu}^3$, and other variables can be found in reference (Yu and Ding, 2003).

In the ABAQUS modeling process, the concrete plastic damage model is selected. The specific definition of concrete plastic damage is shown in Table 3.

3.2 Establishment of finite element model

The fine finite element (FE) models of PSRHSCBs are established by ABAQUS software, as shown in Figure 3. Concrete, H-shaped steels and cushion blocks are established by element C3D8R, and longitudinal steel bars, stirrups and prestressing tendons are established by element T3D2 (Ji et al., 2020). During the process of FE modeling, reinforcement cage, H-shaped steel, and prestressing tendons are embedded in the entire model. The interfacial contact between the H-shaped steel and concrete consisted of hard contact in the normal direction and friction contact with coulomb friction coefficient of 0.5 in the tangent direction. Internal prestressing tendons were embedded in the concrete area at specified position. The two reference points (RP-1 and RP-2) are established at a third of the beams respectively. The RP3 is located on the left side of the beams, and the rotation was set along the x-axis ($U_1 = U_2 = U_3 = UR_2 = UR_3 = 0$). While RP4 is located on the right side of the beams, and the translation is set along the z-axis and the rotation is set along the x-axis ($U_1 = U_2 = UR_2 = UR_3 = 0$). For static analysis, prestressing effect is applied through the temperature reduction method firstly, then the vertical load is applied according to loading rules. During the quasi-static analysis, vertical cyclic load was applied according to cyclic loading rules.

3.3 Verification of finite element model

To verify the rationality of the finite element modeling method, 6 test specimens from reference (Li, 2007), 3 test specimens from reference (Wang et al., 2012), and 2 test specimens from reference (Xue et al., 2007) are selected for finite element simulation, and the specific parameters of existing test specimens are shown in Table 4.

The static analysis of 9 specimens is carried out, and the load-displacement relationship curves of beams under static load are obtained, as shown in Figure 4. It can be seen from Figure 4 that the beams have experienced the elastic stage, the yield stage and the failure stage during the loading process. Since the trend of the load-displacement curves of the finite element simulation is consistent with the trend of the test load-displacement curves, the simulated results are in good agreement with the test results, which confirms

TABLE 4 The specific parameters of existing test specimens.

Specimens	$h \times b$ (mm×mm)	e_H (mm)	S_0	$S_\triangle$		f_{cu}	σ_{con}	L (mm)	N_t (KN)	N_s (KN)	$\frac{\lvert N_s - N_t \rvert}{N_t}$
				Up	Down						
SB-1	220 × 320	0	φ8@150	2Φ18	2Φ18	C50	—	3,200	314	335	6.69 %
PSB-1a	220 × 320	0	φ8@100	2Φ18	2Φ18	C50	$0.65f_{ptk}$	3,200	418	440	5.26 %
PSB-1b	220 × 320	0	φ8@100	2Φ18	2Φ18	C50	$0.7f_{ptk}$	3,200	407	436	7.13 %
SB-2	220 × 400	40	φ8@120	4Φ18	2Φ18	C50	—	3,200	484	498	2.89 %
PSB-2a	220 × 400	40	φ8@80	4Φ18	2Φ18	C50	$0.65f_{ptk}$	3,200	642	668	4.05 %
PSB-2b	220 × 400	40	φ8@80	4Φ18	2Φ18	C50	$0.7f_{ptk}$	3,200	639	659	3.13 %
I-2	200 × 300	0	①	2Φ14	2Φ14	C100	$0.7f_{ptk}$	4,000	260L	270	3.85 %
I-3	200 × 300	0	①	2Φ14	2Φ14	C100	$0.8f_{ptk}$	4,000	254	269	5.91 %
I-4	200 × 300	0	①	2Φ14	2Φ18	C100	$0.7f_{ptk}$	4,000	269	287	6.69 %
PSRCB-1	200 × 300	0	φ8@200	2Φ12	2Φ12	C40	$0.75f_{ptk}$	4,200	—	—	—
PSRCB-2	200 × 300	0	φ8@200	2Φ12	2Φ12	C40	$0.75f_{ptk}$	4,200	—	—	—

Note: ①The stirrup at the bearing is φ8@50, the shear span stirrup is φ8@150, and The pure bending section stirrup is φ8@200.

the accuracy of the constitutive model of the materials. Comparing the numerical simulation value of the ultimate bearing capacity with the experimental ultimate bearing capacity, it is found that the error between the simulated value and the experimental value is small, and the average relative error is about 5%, as shown in Table 4. Then, the quasi-static analysis of the two test specimens is carried out, and the overall trends of the simulated skeleton curve and hysteresis curve are in good agreement with the experimental results, as shown in Figure 5, which verifies the rationality of the finite element modeling method in this paper.

4 The seismic behaviour of 13 PSRHSCBs under low cyclic loading

4.1 Loading scheme

The specimens are subjected to displacement loading, and the cyclic displacement loading is applied at three points along the beams. The mechanical model of PSRHSCBs is shown in Figure 6A, and the loading scheme describing cyclic displacement loading is shown in Figure 6B. Each level of load undergoes a cycle before reaching the yield displacement (denoted as δ). After completing two cycles and reaching the yield displacement load, the specimens are loaded with a multiple of the yield displacement load until they are destroyed. Where n denotes the number of loading cycles.

4.2 Hysteretic curves

The hysteretic curves of PSRHSCBs are shown in Figure 7. It can be seen from that the hysteretic curves of 13 PSRHSCBs show a relatively full shuttle shape, indicating that the PSRHSCBs have excellent seismic behavior. In the process of applying cyclic load, the process from the elastic stage to yield and finally to bearing capacity decline can be clearly obtained. By observing the hysteretic curves shown in Figure 7, it can be found that the e_H and p have a great influence on the hysteretic curves of PSRHSCBs. With the increasing of e_H, the bearing capacity of the beam degrades obviously. With the increase of p, the peak load and corresponding displacement of the hysteresis curve increase obviously, and the ductility increases significantly. This is because when the resistance of the beam section remains unchanged, the increase of p, which makes the bearing capacity of the beam increase.

4.3 Skeleton curves

The load-displacement (P-Δ) skeleton curves of 13 groups of PSRHSCB specimens are shown in Figure 8, and the skeleton curves of all specimens conform to the rule of three broken lines in the elastic stage, elastic-plastic stage, and descending stage. When the L/H decreases from 9.375 to 8.300 and 7.500 in turn, the bearing capacity of composite beams under positive and negative loads increases gradually, as shown in Figure 8A. It can be seen from Figure 8C, with the increasing of p_v, the initial stiffness of the specimens gradually decreases, the peak load increases greatly, and the falling section of the skeleton curves tends to be flattened, which is showing excellent load holding capacity. It can be seen from Figure 8D that with the increasing of e_H, the bearing capacity of PSRHSCBs decreases significantly. Figures 8B, E, F show that the influences of f_{cu}, p, and σ_{con} on the peak load of the skeleton curves for PSRHSCBs are not obvious.

4.4 Degradation of stiffness

During repeated loading of structures, the degradation of stiffness can be expressed by secant stiffness (K_i) (Ji et al., 2021a), which could be expressed by Eq. 9.

$$K_i = \frac{|+F_i| + |-F_i|}{|+\Delta_i| + |-\Delta_i|} \tag{9}$$

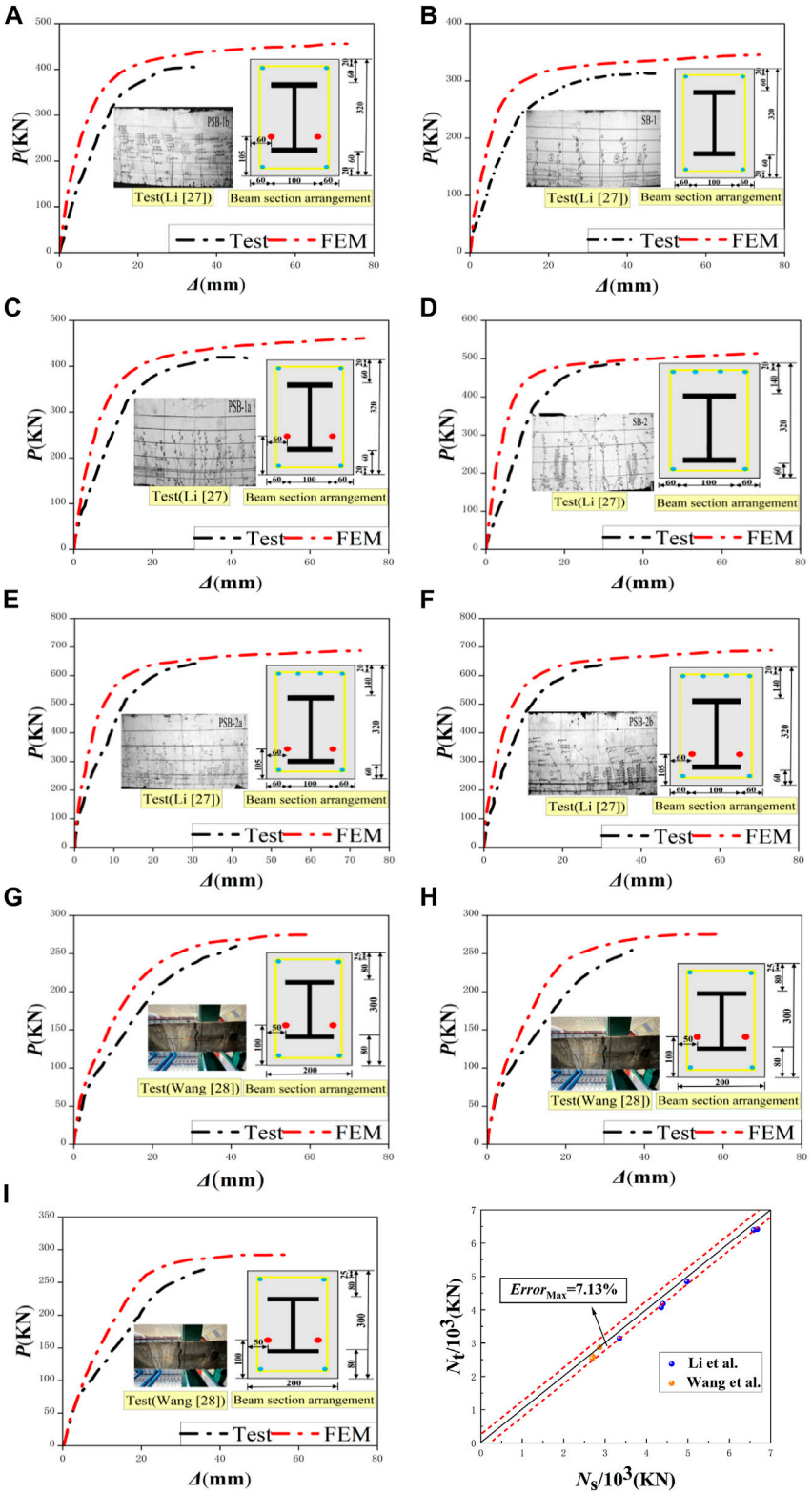

FIGURE 4
(1) Numerical simulation of 9 test pieces and test load and displacement relationship curves: **(A)** SB-1; **(B)** PSB-1a; **(C)** PSB-1b; **(D)** SB-2; **(E)** PSB-2a; **(F)** PSB-2b; **(G)** I-2; **(H)** I-3; **(I)** I-4. (2) Comparison of Ns and Nt for nine specimens.

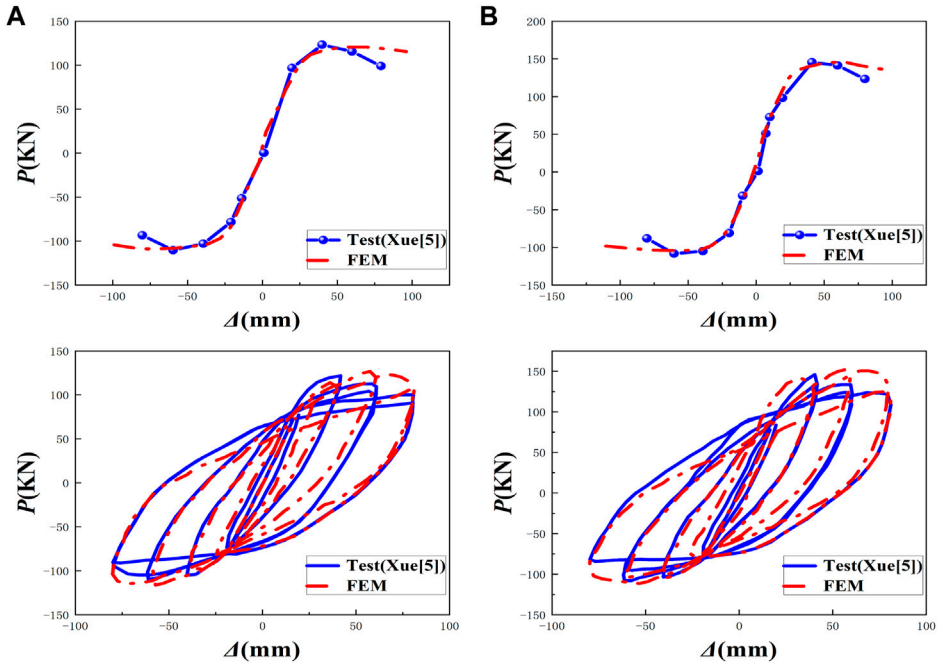

FIGURE 5
(1) Comparison of skeleton curves: **(A)** PSRCB-1; **(B)** PSRCB-2. (2) Comparison of hysteretic curves: **(A)** PSRCB-1; **(B)** PSRCB-2.

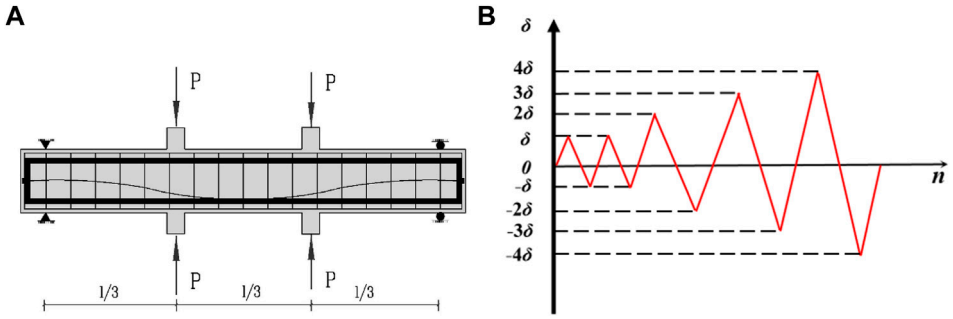

FIGURE 6
(A) The mechanical model of beams; **(B)** Reciprocating loading scheme.

Where F_i denotes the peak horizontal load of the first cycle under the i-th control displacement and Δ_i refers to the corresponding displacement.

The secant stiffness comparisons of 13 PSRHSCBs with different parameters are shown in Figure 9. The K_i decreases with the increasing of horizontal displacement (Δ), and its decreasing range gradually slows down with the increase of Δ. It can be seen from Figure 9 that with the decreasing of σ_{con} and L/H, the initial stiffness and declining degree of secant stiffness increase gradually. When σ_{con} reaches $0.7f_{ptk}$, the deformation resistance decreases seriously, which indicates that σ_{con} should not less than $0.7f_{ptk}$. The e_H has a significant effect on the secant stiffness of specimens. With the increase of e_H, the initial stiffness of the specimens increases obviously, and the stiffness degradation phenomenon becomes faster. The effects of f_{cu}, p_v, and p on the stiffness degradation of specimens are not obvious.

4.5 Energy dissipation capacity

The energy dissipation capacity is applied to evaluate the ability to absorb the energy released in the earthquake of the structure (Cai et al., 2021). The energy dissipation coefficient (E) is used to evaluate the energy dissipation capacity of PSRHSCB specimens, and the energy dissipation coefficient refers to the ratio of the shadow area to the triangle DFO and the triangle BEO area, as shown in Figure 10 (1).

The energy dissipation coefficient can be calculated as follows in Eq. 10:

$$E = \frac{S_{(ABC+CDA)}}{S_{(\Delta OBE+\Delta ODF)}} \tag{10}$$

Figure 10 (2) shows the horizontal displacement (Δ) *versus* the energy dissipation coefficient (E) relationships of the 13 PSRHSCBs

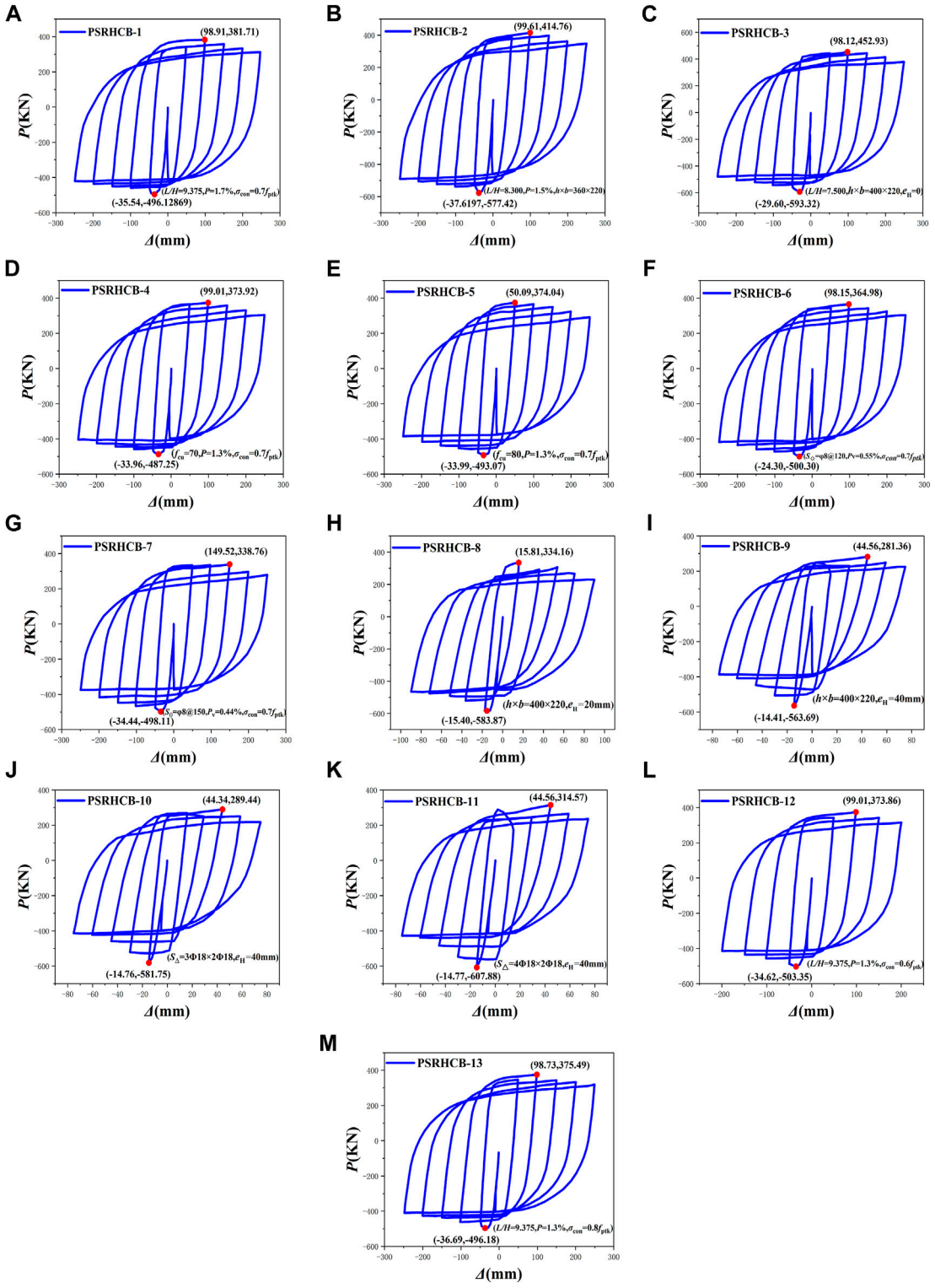

FIGURE 7
Load-displacement hysteretic curves of 13 PSRHSCB specimens: **(A)** PSRHSCB-1; **(B)** PSRHSCB-2; **(C)** PSRHSCB-3; **(D)** PSRHSCB-4; **(E)** PSRHSCB-5; **(F)** PSRHSCB-6; **(G)** PSRHSCB-7; **(H)** PSRHSCB-8; **(I)** PSRHSCB-9; **(J)** PSRHSCB-10; **(K)** PSRHSCB-11; **(L)** PSRHSCB-12; **(M)** PSRHSCB-13.

under the first reciprocating load of each stage. It can be found from Figure 10 (2) that the energy dissipation capacity values of the 13 PSRHSCBs are substantially similar.

The energy dissipation capacity of PSRHSCBs is shown in Figure 10 (2). With the increase of f_u, the energy dissipation capacity of the specimen decreases gradually, while with the

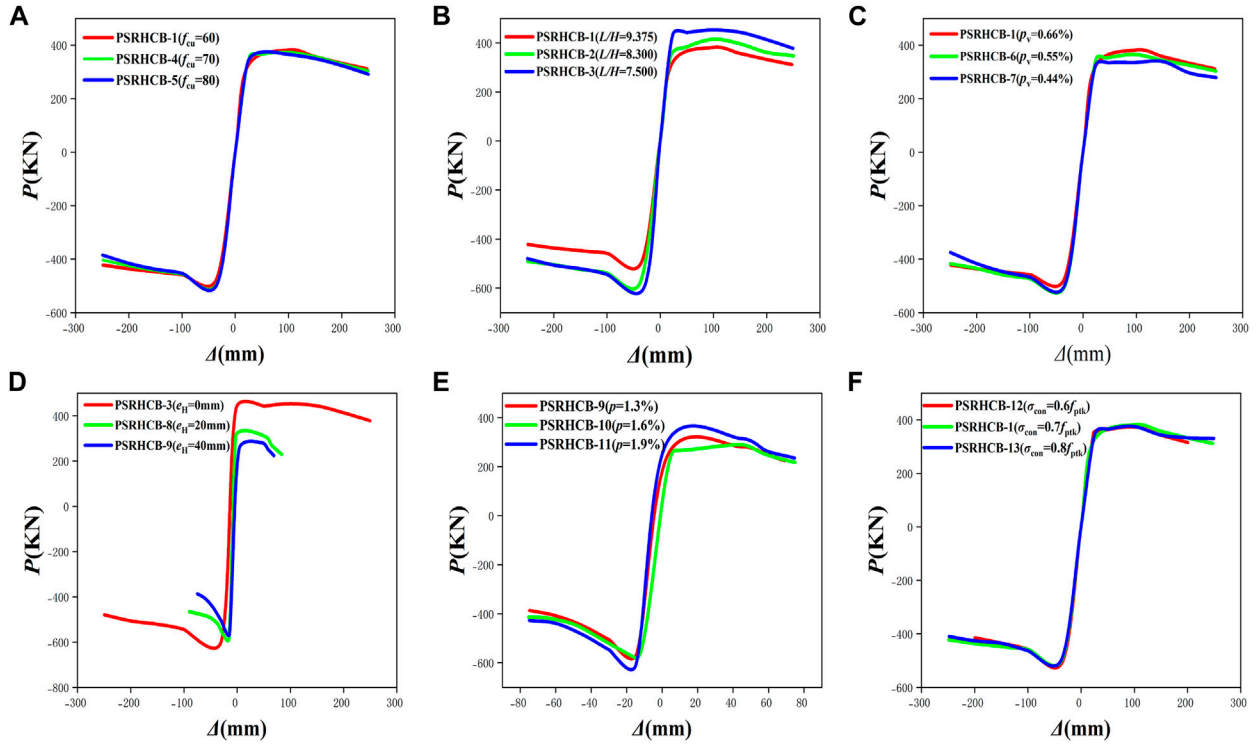

FIGURE 8
Skeleton curves of PSRHSCBs with different parameters: **(A)** L/H; **(B)** f_{cu}; **(C)** p_v; **(D)** e_H; **(E)** p; **(F)** σ_{con}.

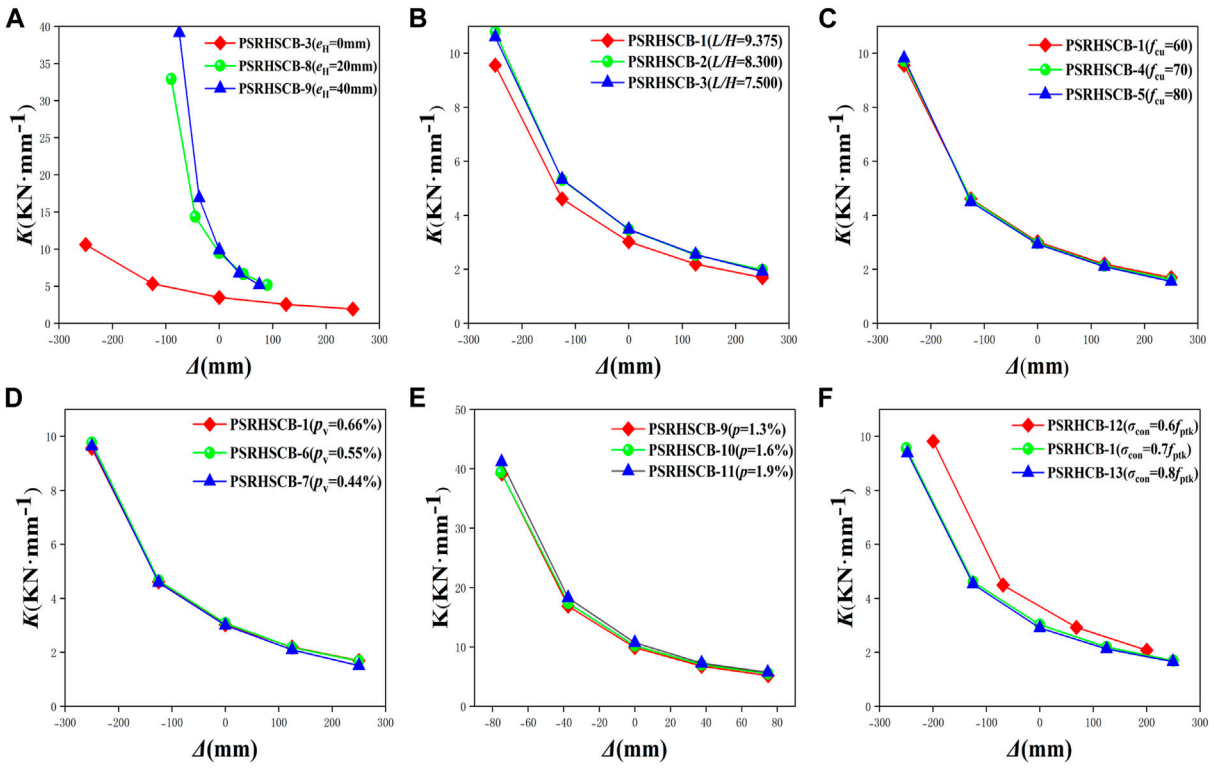

FIGURE 9
The relationships between K_i and Δ for PSRHSCB specimens with different parameters: **(A)** L/H; **(B)** f_{cu}; **(C)** p_v; **(D)** e_H; **(E)** p; **(F)** σ_{con}.

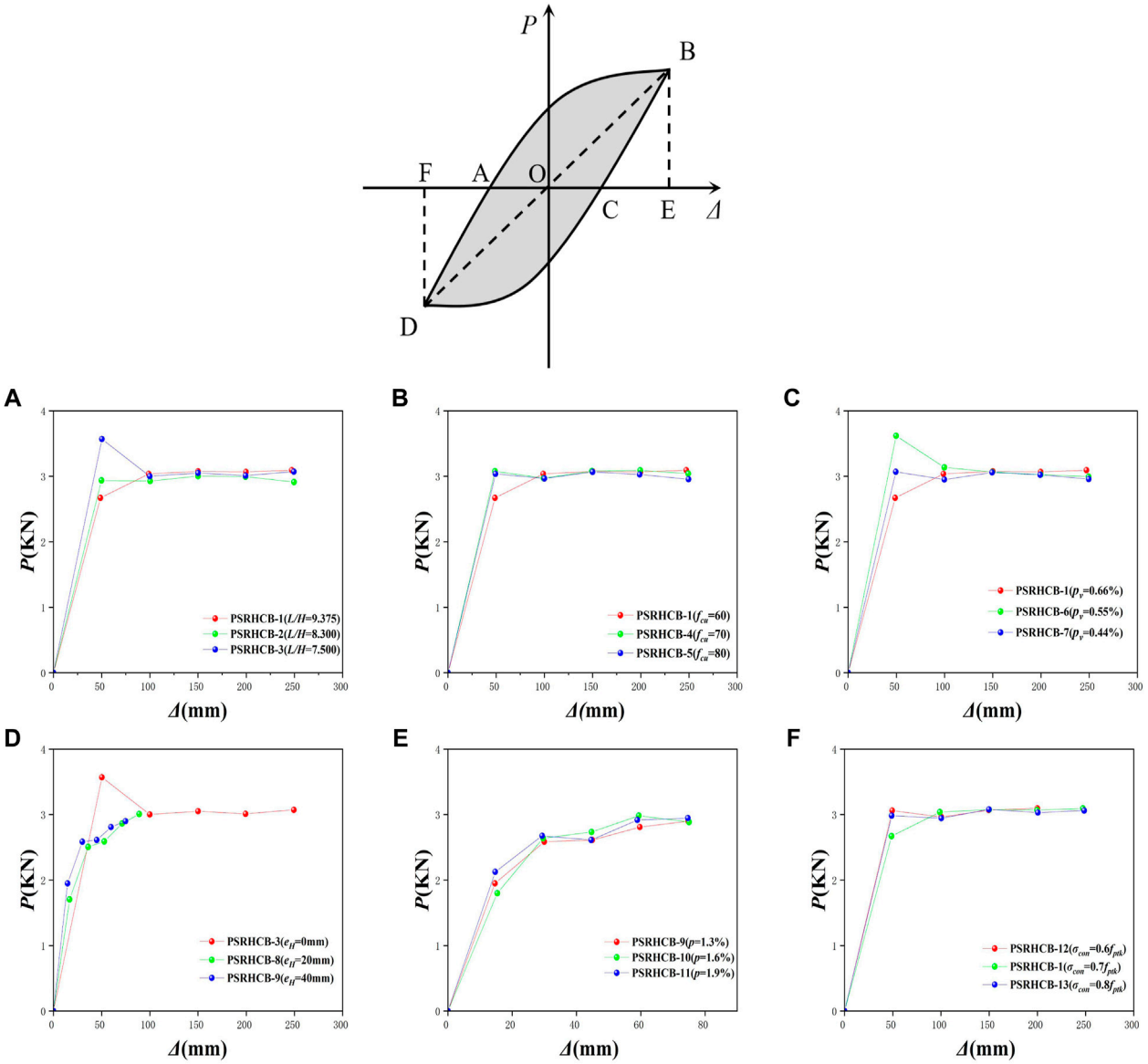

FIGURE 10
(1) Calculation diagram of *E*. (2) Comparisons of energy dissipation capacity for PSRHSCB specimens with different parameters: **(A)** *L/H*; **(B)** f_{cu}; **(C)** p_v; **(D)** e_H; **(E)** *p*; **(F)** σ_{con}.

increase of *L/H* and p_v, the energy dissipation capacity of the specimen increases gradually. It can be seen from Figure 10 (2) (D) that E_H has a great influence on the energy dissipation capacity of PSRHSCBs.When the H-shaped steels are eccentrically arranged, the energy dissipation capacity is poor. It can be seen from Figures 10 E, F (2) that *p* and σ_{con} have little effect on the energy dissipation capacity of PSRHSCBs. The *E* of most of the specimens in this paper can reach more than 2.0, indicating that PSRHSCBs have excellent energy dissipation capacity.

4.6 Ductility

Ductility is regarded as the main parameter to measure the deformation performance of the specimens (Ji et al., 2021b), and it can be explained by the ductility coefficient (μ), which can be calculated by Eq. 11.

$$\mu = \Delta_u / \Delta_y \tag{11}$$

Where Δ_u refers to the ultimate displacement and Δ_y denotes the yield displacement.

Based on the *P-Δ* curves, the equivalent yield point can be obtained by finding the corresponding point of 0.7 times as P_{max} on the curves, and the yield load (P_y) can be calculated, as shown in Figure 11 (1) The peak displacement (Δ_{max}), yield displacement, ultimate displacement, and ductility coefficient of the specimens are shown in Table 5. The relationships between μ and *L/H*, f_{cu}, p_v, e_H, σ_{con}, and *p* of the PSRHSCB specimens are shown in Figure 11 (2). It can be seen from Figure 11 (2) that the μ of the PSRHSCB$_S$

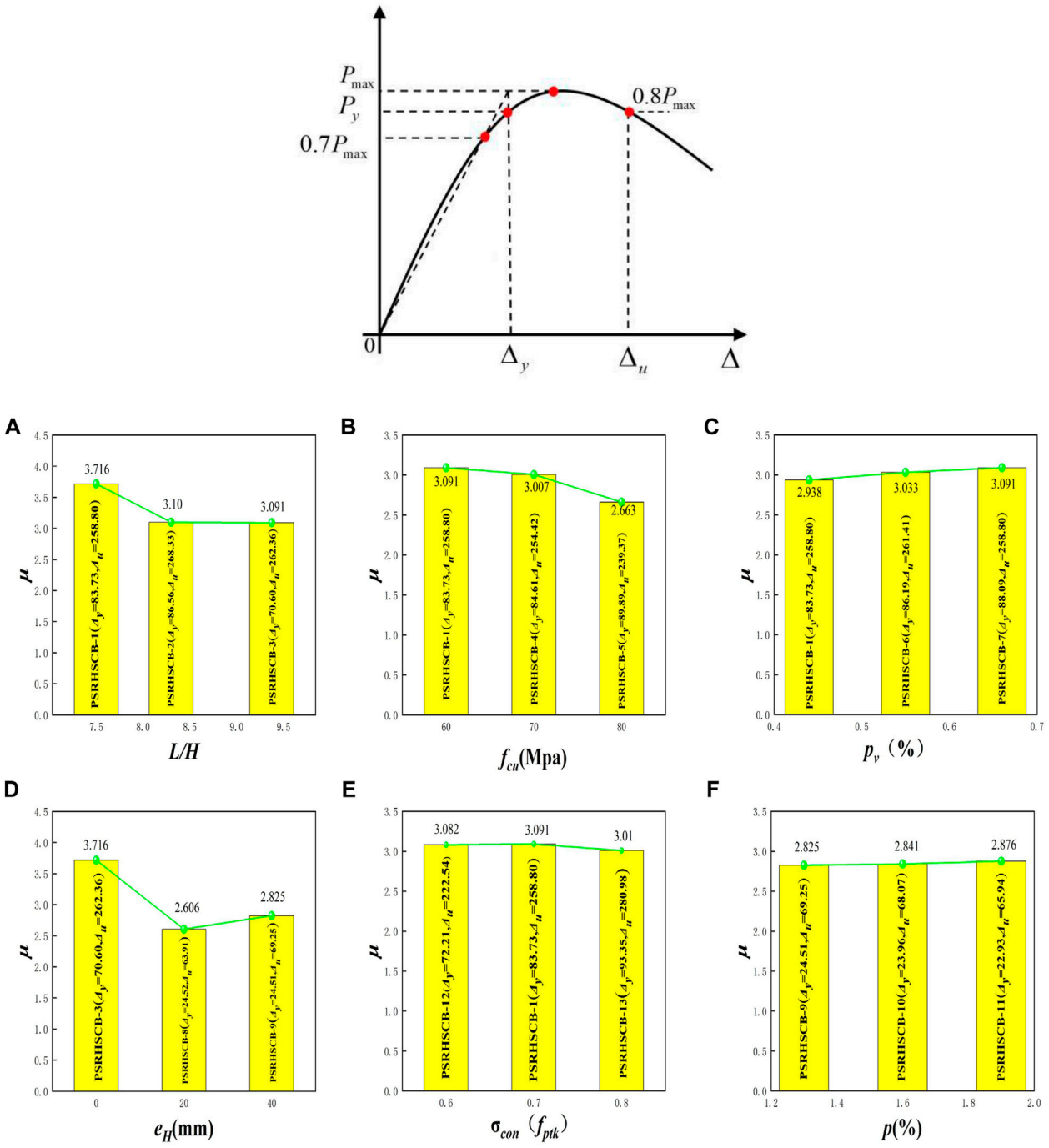

FIGURE 11
(1) The yield displacement obtained by the R.Park method. (2) The relationships between different parameters and μ for PSRHSCB specimens: **(A)** L/H; **(B)** f_{cu}; **(C)** p_v; **(D)** e_H; **(E)** σ_{con}; **(F)** p.

increases gradually with the decreasing of L/H and f_{cu}. When the L/H decreases from 9.375 to 8.300 and 7.500 in turn, μ increases from 3.091 to 3.100 and 3.716, which increases by 3.16% and 20.23%, respectively. When the f_{cu} decreases from 80Mpa to 70 Mpa and 60 Mpa in turn, μ increases from 2.663 to 3.007 and 3.091, which increases by 12.92% and 16.07%, respectively. So, it can be found that L/H and f_{cu} have significant effects on the ductility of specimens. By consulting the relevant literature, the ductility coefficient of reinforced concrete seismic structures in general engineering is in the range of 3–4. Among the ductility coefficients of 13 specimens calculated by the R-park method, 7 specimens are greater than 3, and the remaining 6 specimens are above 2.6. The six components that do not reach 3 are due to the excessive concrete strength (PSRHSCB-5), the excessive tension control stress (PSRHSCB-7), and the torsion of steel eccentricity (PSRHSCB-8,9,10,11).

TABLE 5 The ductility coefficients of 13 PSRHSCB specimens.

Specimens	P_{max} (MPa)	Δ_{max} (mm)	P_y (MPa)	Δ_y (mm)	Δ_u (mm)	μ
PSRHSCB-1	381.71	247.26	364.25	83.73	258.80	3.091
PSRHSCB-2	414.76	250.27	403.62	86.56	268.33	3.100
PSRHSCB-3	452.93	249.17	443.39	70.60	262.36	3.716
PSRHSCB-4	373.92	249.73	365.302	84.61	254.42	3.007
PSRHSCB-5	374.04	249.88	363.43	89.89	239.37	2.663
PSRHSCB-6	364.98	249.61	359.39	86.19	261.41	3.033
PSRHSCB-7	338.76	249.98	329.21	88.09	258.80	2.938
PSRHSCB-8	334.16	83.39	324.26	24.52	63.91	2.606
PSRHSCB-9	281.36	69.02	262.50	24.51	69.25	2.825
PSRHSCB-10	289.44	74.85	269.57	23.96	68.07	2.841
PSRHSCB-11	314.57	74.66	294.00	22.93	65.94	2.876
PSRHSCB-12	373.86	200.32	369.34	72.21	222.54	3.082
PSRHSCB-13	375.49	249.36	371.52	93.35	280.98	3.010

4.7 Failure modes of this kind of thirteen PSRHSCBs

The failure modes of PSRHSCBs under low cyclic vertical loading are analyzed in this paper. The bending failure at the mid-span section of the beam is the mainly failure mode of the specimen, and the maximum strain appears at the mid-span of the beam. Finally, the steel reinforcement cage, H-shaped steel, and prestressing tendons reach the ultimate strain, and the composite beam is destroyed as a whole. The stress distribution of several representative specimens is shown in Figure 12. As shown in Figure 12, the maximum stress of the steel reinforcement cage and the H-shaped steel is occurred in the middle of the beams.

5 Restoring force model

5.1 The ratio coefficient of section stiffness to total section stiffness of H-shaped steel

To establish a load-displacement restoring force model for PSRHSCBs, the ratio coefficient of section steel stiffness to total section stiffness (γ) is introduced, the calculation formulas are as follows (Ji, 2008):

$$\gamma = \frac{B_{ss}}{B_s} \tag{12}$$

$$B_s = B_{prc} + B_{ss} \tag{13}$$

Where, B_{ss} the sectional stiffness of H-shaped steel, B_s is the total stiffness of the beam section, and B_{prc} is the sectional stiffness of reinforced concrete.

$$B_{prc} = 0.85E_0I_0 \tag{14}$$

Where, E_0 is the elastic modulus of concrete, I_0 is the converted section moment of inertia of reinforced concrete.

$$B_{ss} = E_{ss}\left[I_{ss} + A_{ss}\left(y_{ss} - x_0\right)^2\right] \tag{15}$$

Where E_{ss} is the elastic modulus of the section of steel, I_{ss} is the moment of inertia of the section of the steel to its centroid axis, y_{ss} is the distance from the centroid of the section of the steel to the top surface, A_{ss} is the section area of section steel, and x_0 is the distance from the neutral axis to top surface in actual cross-section, calculated according to reference (Zhao et al., 2001).

The γ of 13 specimens is calculated using the above formulas. The values of γ are listed in Table 6.

5.2 Calculation of flexural bearing capacity of normal section

Through the stress nephograms of the finite element model of PSRHSCBs, it can be seen that the H-shaped steel flange yields under both tension and compression. Therefore, the flexural capacity of the normal section of PSRHSCBs is calculated by using the formula proposed in the literature (Ji, 2008). The stress diagram of the H-shaped steel with uniform yield at the flange under tension and compression is shown in Figure 13.

5.3 Verification of trilinear skeleton curve model

According to the characteristics of skeleton curves, the trilinear skeleton curve model of PSRHSCBs is obtained by statistical regression, as shown in Figure 14 (1). Regression is required to determine 5 pairs of reference points: peak load $P_u(P'_u)$, yield load $P_y(P'_y)$, yield displacement $\Delta_y(\Delta'_y)$, peak displacement $\Delta_m(\Delta'_m)$, and descending section stiffness $K_d(K'_d)$.

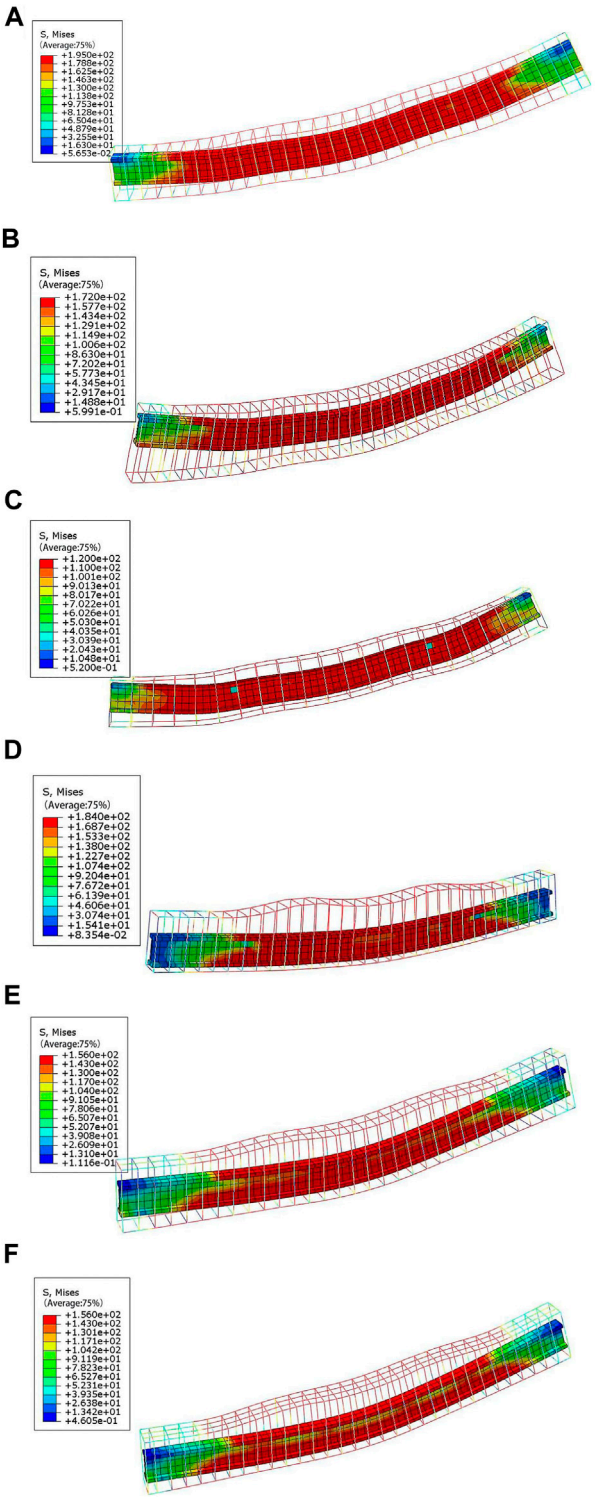

FIGURE 12
The stress distribution of PSRHSCBs: **(A)** PSRHSCB-1; **(B)** PSRHSCB-3; **(C)** PSRHSCB-7; **(D)** PSRHSCB-8; **(E)** PSRHSCB-10; **(F)** PSRHSCB-11.

(1) Numerical analysis regression obtains the expression of the initial section stiffness B_s of the control section in the span of the composite beam as shown in Eq. 16.

TABLE 6 The value of γ of 13 specimens.

Specimens	γ
PSRHSCB-1	0.15
PSRHSCB-2	0.08
PSRHSCB-3	0.07
PSRHSCB-4	0.09
PSRHSCB-5	0.1
PSRHSCB-6	0.15
PSRHSCB-7	0.14
PSRHSCB-8	0.22
PSRHSCB-9	0.38
PSRHSCB-10	0.39
PSRHSCB-11	0.4
PSRHSCB-12	0.14
PSRHSCB-13	0.15

$$B_s = (0.7 + \lambda^{0.4})B_{prc} + 0.45B_{ss} - 259398 \tag{16}$$

Where, λ is the ratio of shear span to depth, B_{ss} is the sectional stiffness of H-shaped steel, and B_{prc} is the sectional stiffness of reinforced concrete.

The Initial stage stiffness expression of components (Ji et al., 2021a) is shown in Eq. 17.

$$K_e = 24B_s/b(3L^2 - 4b^2) \tag{17}$$

Where, L is the span of the beam, and b is the concentration of the distance from the loading point to the bearing.

(2) The peak load is shown in Eq. 18.

$$\begin{cases} P_u = M_u/(L/2 - D/2) \\ P_u' = -(0.76 + 2.1\lambda^{2.2})P_u - 154 \end{cases} \tag{18}$$

Where, D is the distance between two loading points, P_u is the ultimate load when subjected to upward loads; P_u' is the ultimate load when subjected to downward loads.

(3) The yield load is shown in Eq. 19.

$$\begin{cases} P_y = (0.72 + 0.14\lambda^2)P_u \\ P_y' = (0.9 - 1.5\lambda^3)P_u' \end{cases} \tag{19}$$

Where P_y is yield load when subjected to upward load; P_y' is Yield loads when subjected to downward loads.

(4) Yield displacement is shown in Eq. 20.

$$\begin{cases} \Delta_y = P_y/K_e \\ \Delta_y' = P_y'/K_e \end{cases} \tag{20}$$

Where Δ_y is P_y corresponding displacement, Δ_y' is P_y' corresponding displacement.

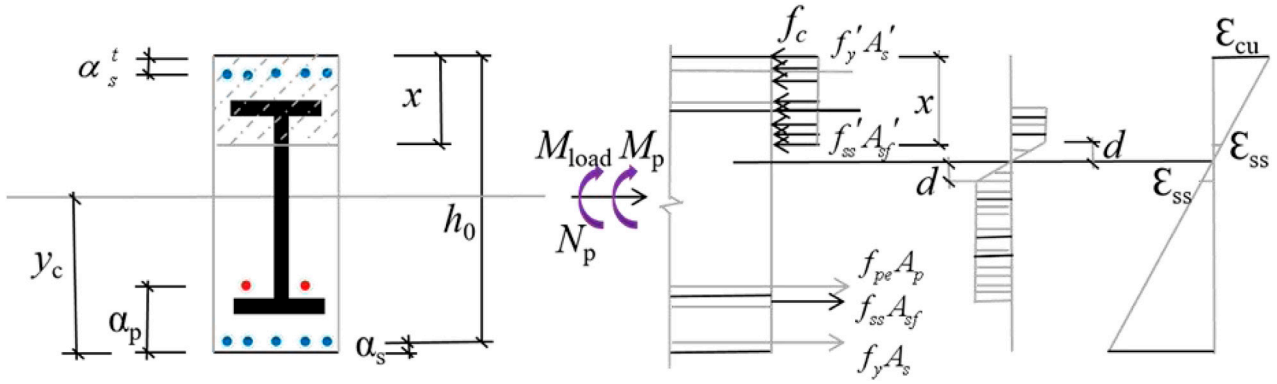

FIGURE 13
Stress diagram for yielding of H-shaped steel flanges under tension and compression.

(5) Peak displacement is shown in Eq. 21.

$$\begin{cases} \Delta_m = (1.7 + 11.3\lambda^2)\Delta_y \\ \Delta_m^{'} = (2 + 0.4\lambda^{2.5})\Delta_y^{'} \end{cases} \tag{21}$$

Where Δ_m is peak displacement when subjected to upward loads, Δ_m' is peak displacement when subjected to downward loads.

(6) Falling section stiffness is shown in Eq. 22.

When the bearing capacity drops to 85% of the ultimate bearing capacity, the specimen reaches failure.

$$\begin{cases} K_d = \dfrac{0.85P_u - P_u}{\Delta_y - \Delta_m} \\ K_d^{'} = \dfrac{0.85P_u^{'} - P_u^{'}}{\Delta_y^{'} - \Delta_m^{'}} \end{cases} \tag{22}$$

Where Δ_y is $0.85P_u$ Corresponding displacement, Δ_y' is 0.85 P_u' Corresponding displacement.

Regression gets Eq. 23.

$$\begin{cases} K_d = (0.123 + 0.018\lambda^{-2} + 0.095\lambda^{-4})K_e - 0.37 \\ K_d^{'} = (0.08 + 0.42\lambda^{-2.5} - 0.05\lambda^{-3} - 0.25\lambda^{-5.5})K_e - 0.25 \end{cases} \tag{23}$$

(7) Verification of trilinear skeleton curve model.

The comparisons of the simulated and calculated skeleton curves are shown in Figure 14 (2). It can be found that the skeleton curves obtained by equation are in good agreement with the numerical simulation results, which can provide a reference for engineering design.

5.4 Hysteretic rule of restoring force model

The restoring force model (RFM) of PSRHSCB is established by statistical regression, as shown in Figure 15 (1), where the numbers: 0, 1, 2, . . . , express the walking routes of the model in the process of loading and unloading in forward-backward directions (Ji et al., 2022). The hysteretic curves of 13 specimens were observed, and it was found that the forward and reverse loading paths approximately passed through a "fixed point". The statistical analysis of the experimental data showed that the fixed point was the intersection of the loading path and the elastic section in the positive and reverse directions, and the ordinates were 0.65 P_u and-0.65 P_u, respectively.

The hysteretic rules are expressed as follows:

(1) Loading and unloading rules of elastic stage

Before the restoring force reaches P_y, the loading is carried out along the skeleton curve. During unloading, the initial stiffness is taken into account, regardless of stiffness degradation and residual deformation.

(2) Loading and unloading rules of elastoplastic stage

When the restoring force exceeds the horizontal yielding load P_y in the forward or backward direction, but is smaller than the peak load P_u, loading occurs along the skeleton curve, whereas unloading conforms to Eq. 24, and the unloading stiffness (K_{un}) is developed through regression analysis.

$$K_{un} = 3.2117\left(\frac{\Delta_{un}}{\Delta_y}\right)^{-0.2192} K_e \tag{24}$$

Where Δ_y is the yielding displacement, Δ_{un} is the displacement at the unloading point, and K_e is the initial stiffness.

(3) Loading-unloading rules at the descending segment stage

When the restoring force exceeds P_u in the forward or backward direction, K_d in descending segment stage of the skeleton curve is taken as the loading stiffness and unloading stiffness is still calculated according to Eq. 24.

(4) Backward loading and forward reloading rules

In the case of backward loading after forward unloading, when the maximum displacement in the backward direction does not

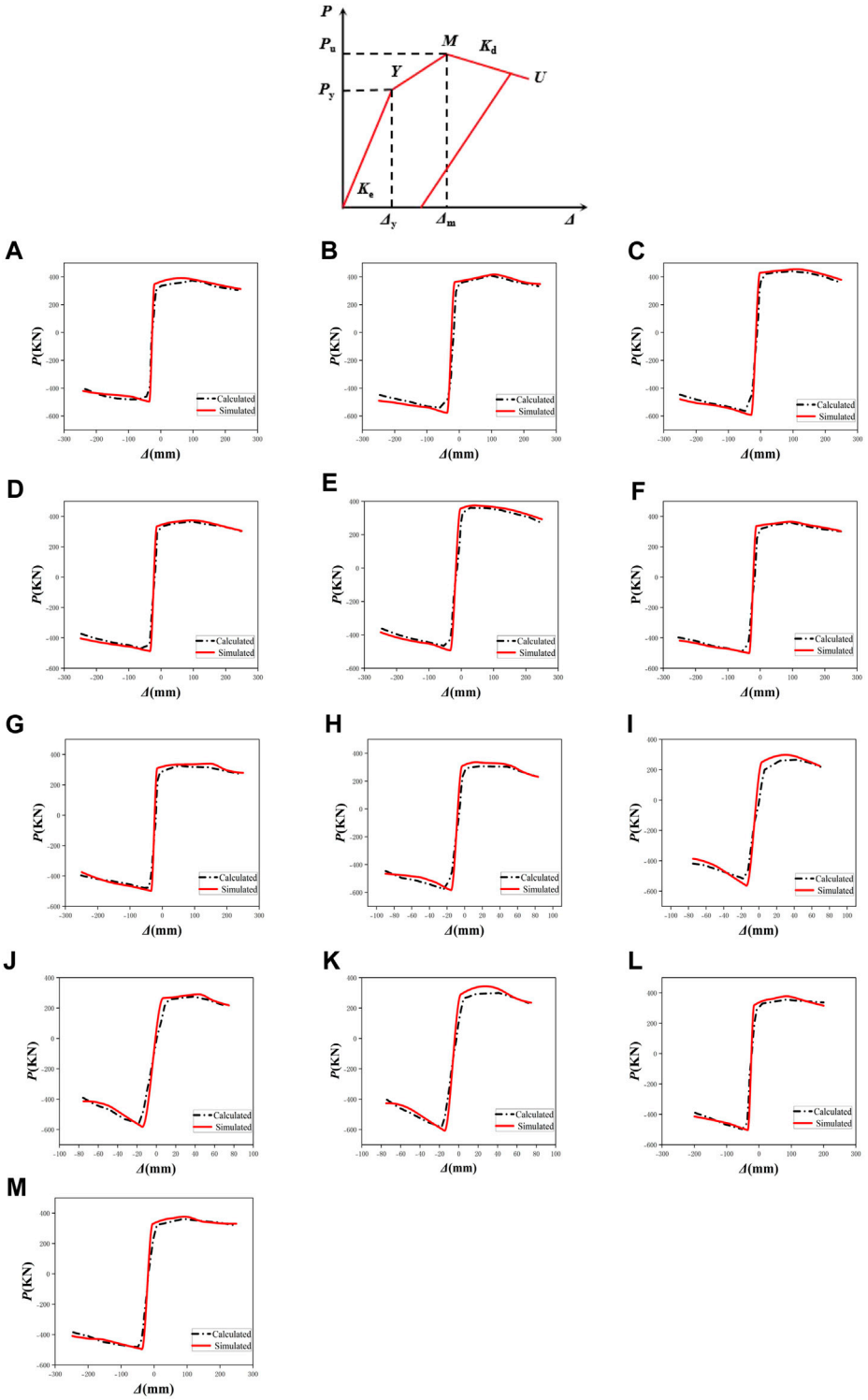

FIGURE 14
(1) Trilinear skeleton curve model. (2) Comparison between simulated and calculated skeleton curves: **(A)** PSRHSCB-1; **(B)** PSRHSCB-2; **(C)** PSRHSCB-3; **(D)** PSRHSCB-4; **(E)** PSRHSCB-5; **(F)** PSRHSCB-6; **(G)** PSRHSCB-7; **(H)** PSRHSCB-8; **(I)** PSRHSCB-9; **(J)** PSRHSCB-10; **(K)** PSRHSCB-11; **(L)** PSRHSCB-12; **(M)** PSRHSCB-13.

exceed the yield displacement, the walking route is from the point of $p = 0.65P_u$ directly to the yielding point in the backward direction. When the maximum displacement in the backward direction exceeds the yielding displacement, the walking route is from the point of $p = 0.65P_u$ to the maximum displacement point in the backward direction. For forward reloading after backward unloading, the walking route is from the point of $p = 0.65P_u$ to the maximum point in the forward direction.

10.3389/fmats.2023.1267961

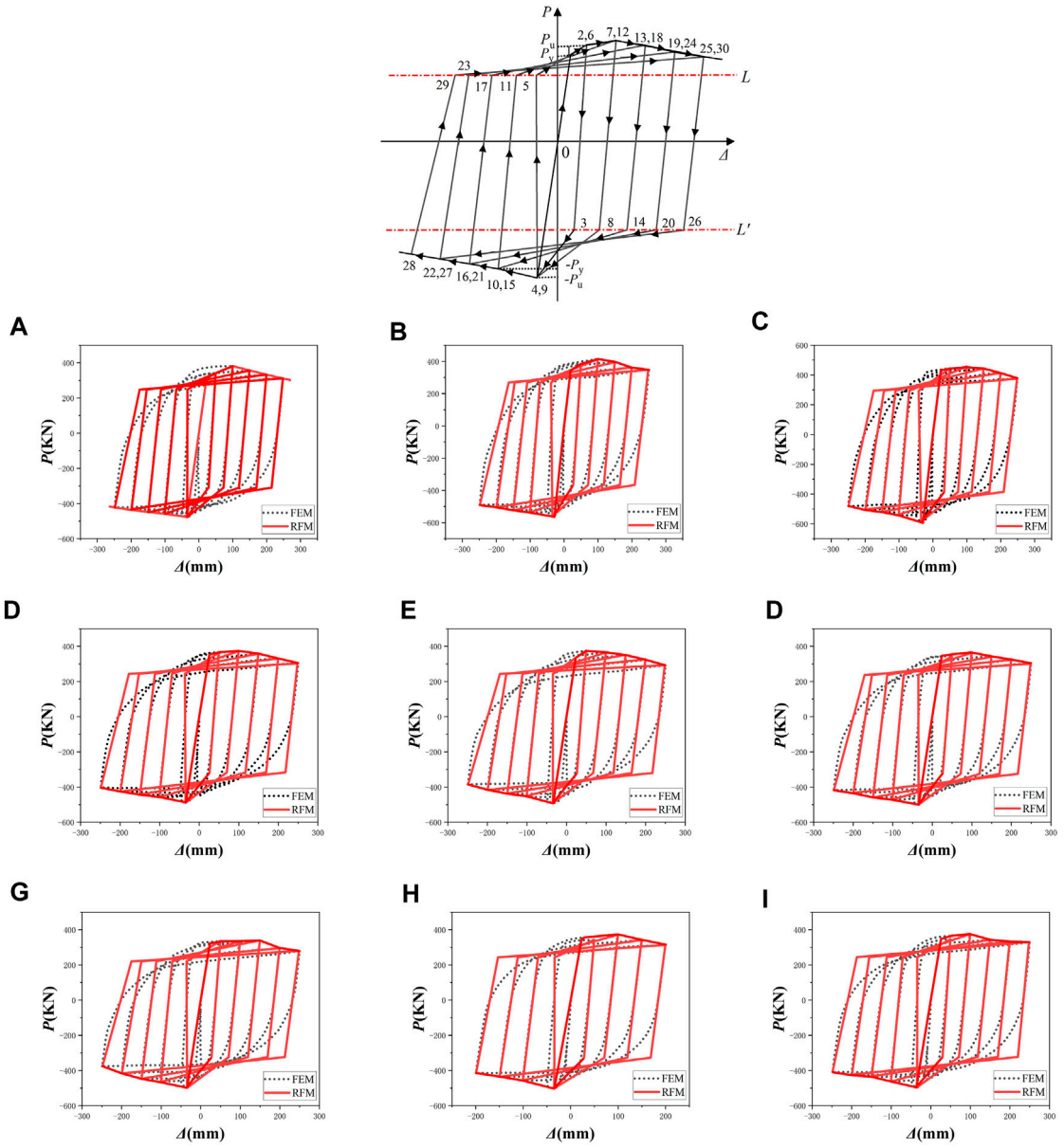

FIGURE 15
(1) Restoring force model for PSRHSCBs. (2) Comparisons between the hysteretic curves obtained by FES and RFM: **(A)** PSRHSCB-1; **(B)** PSRHSCB-2; **(C)** PSRHSCB-3; **(D)** PSRHSCB-4; **(E)** PSRHSCB-5; **(F)** PSRHSCB-6; **(G)** PSRHSCB-7;**(H)** PSRHSCB-12; **(I)** PSRHSCB-13.

The comparisons between the hysteretic curves obtained by finite element simulation (FES) and RFM are shown in Figure 15 (2), and it can be seen that both of them are in good agreement, therefore, the restoring force model of this kind of composite beam is reasonable.

6 Conclusion

To investigate the seismic behavior of PSRHSCBs under low cyclic loading, Thirteen groups of PSRHSCB specimens were designed with different parameters. These parameters included the span-to-height ratio of beams (L/H), the cubic strength of the concrete (f_{cu}), the eccentricity of the H-shaped steel (e_H), the volume stirrup ratio (p_v), the longitudinal reinforcement ratio (p), and tension control stress of tendons(σ_{con}). Then, the finite element models of 13 PSRHSCBs were established by ABAQUS software. By analyzing the data within the parameter range, the following conclusions can be drawn:

(1) Based on the concrete constitutive model proposed by Ding and Yu, and the prestressing effect applied by temperature reduction method, the finite element models of 13 PSRHCBs were established by using ABAQUS software with reasonable finite element method.
(2) The hysteresis curves of the 13 specimens showed obvious shuttle shape and no pinch phenomenon occurred, which

indicates that the structure showed good seismic behavior. Additionally, the skeleton curves of the 13 specimens follow the trilinear rule in the elastic stage, elastic-plastic stage, and descending stage, showing excellent bearing capacity and ductility. The peak load of the skeleton curve increases with the increase of f_{cu}, p_v, p, and σ_{con}, and decreases with the increase of L/H and e_H, and L/H, p_v and e_H have more significant effects on the peak load of this kind of novel PSRHSCBs.

(3) The stiffness degradation of PSRHSCBs is significantly influenced by the parameters of e_H. Decreasing e_H can improve the stiffness degradation of specimens significantly. In addition, the energy dissipation capacity of the specimens increases with the rising of p_v and p, and gradually decreases with the rising of L/H and f_{cu}. The L/H, e_H and σ_{con} have a great influence on the ductility. With the increase of L/H, the ductility of the specimen decreases gradually. With the increase of e_H, the ductility of the specimen decreases first and then increases. On the contrary, with the increase of σ_{con}, the ductility of the specimen increases first and then decreases. In addition, with the increase of σ_{con}, the energy dissipation capacity of specimens increases firstly, and when σ_{con} exceeds 0.7 f_{ptk}, the energy dissipation capacity decreases gradually. When e_H increases, the energy dissipation capacity of specimens decreases greatly.

(4) Based on the hysteresis curves obtained by the quasi-static analysis, the trilinear skeleton curve model and the corresponding restoring force model are established, and the hysteresis rules are proposed correspondingly, and the skeleton curves and hysteretic curves obtained by equation are in good agreement with the numerical simulation results, indicating that the restoring force model is reasonable and feasible.

Data availability statement

The original contributions presented in the study are included in the article/Supplementary Material, further inquiries can be directed to the corresponding authors.

Author contributions

JH: Software, Validation, Writing–original draft, Writing–review and editing. LJ: Writing–review and editing. JJ: Supervision, Writing–review and editing. ZZ: Writing–review and editing. CX: Writing–review and editing. HY: Writing–review and editing. HZ: Writing–review and editing.

Funding

The author(s) declare financial support was received for the research, authorship, and/or publication of this article. This work is supported by Joint Guidance Project of Natural Science Foundation of Heilongjiang Province (No. LH 2020E018), Scientific Research Fund of Institute of Engineering Mechanics of China Earthquake Administration (No. 2020D07), China-Pakistan Belt and Road Joint Laboratory on Smart Disaster Prevention of Major Infrastructures (No. 2022CPBRJL-05), Northeast Petroleum University Guided Innovation Fund (No. 2020YDL-02), Guiding Science and Technology Project of Daqing City (No. zd-2021-40).

Conflict of interest

The authors declare that the research was conducted in the absence of any commercial or financial relationships that could be construed as a potential conflict of interest.

Publisher's note

All claims expressed in this article are solely those of the authors and do not necessarily represent those of their affiliated organizations, or those of the publisher, the editors and the reviewers. Any product that may be evaluated in this article, or claim that may be made by its manufacturer, is not guaranteed or endorsed by the publisher.

References

Ahmad, S. H., and Shah, S. P. (1985). Structural properties of high strength concrete and its implications for precast prestressed concrete. *PCI J.* 30 (6), 92–119. doi:10.15554/pcij.11011985.92.119

Akiyama, M., Abe, S., Aoki, N., and Suzuki, M. (2012). Flexural test of precast high-strength reinforced concrete pile prestressed with unbonded bars arranged at the center of the cross-section. *Eng. Struct.* 34, 259–270. doi:10.1016/j.engstruct.2011.09.007

Aleksandrova, N. (2012). Application of mises yield criterion to rotating solid disk problem. *Int. J. Eng. Sci.* 51, 333–337. doi:10.1016/j.ijengsci.2011.10.006

Cai, Z., Liu, F., Yu, J., Yu, K., and Tian, L. (2021). Development of ultra-high ductility engineered cementitious composites as a novel and resilient fireproof coating. *Constr. Build. Mater.* 288, 123090. doi:10.1016/j.conbuildmat.2021.123090

Ding, F. X., and Yu, Z. W. (2004). Unified calculation method of mechanical properties of concrete in tensile. *J. Huazhong Univ. Sci. Technol.*

Graybeal, B. A. (2008). Flexural behavior of an ultrahigh-performance concrete i-girder. *J. Bridge Eng.* 13 (6), 602–610. doi:10.1061/(ASCE)1084-0702(2008)13:6(602)

Han, L. H., Tao, Z., and Liu, W. (2001). Concrete filled steel tubular structures from theory to practice. *J. Fuzhou Univ. Sci.* 29 (6), 24–34. doi:10.3969/j.issn.1000-2243.2001.06.004

Ji, J., He, L., Jiang, L., Lin, Y., Ni, S., Wang, Z., et al. (2021a). Seismic behavior of gfrp tube reactive powder concrete composite columns with encased steel. *Front. Mater.* 8. doi:10.3389/fmats.2021.793392

Ji, J., He, L., Jiang, L., Zhang, Y., Liu, Y., Li, Y., et al. (2023b). Numerical study on the axial compression behavior of composite columns with steel tube SHCC flanges and honeycombed steel web. *Eng. Struct.* 283, 115883. doi:10.1016/j.engstruct.2023.115883

Ji, J., Li, Y. H., Jiang, L. Q., Zhang, Y. F., Liu, Y. C., He, L. J., et al. (2023a). Axial compression behavior of strength-gradient composite stub columns encased CFST with small diameter: experimental and numerical investigation. *Structures* 47, 282–298. doi:10.1016/j.istruc.2022.11.069

Ji, J., Lin, Y., Jiang, L., Li, W., Yu, C., Wang, R., et al. (2022). Hysteretic behavior of h-shaped honeycombed steel web composite columns with rectangular concrete-filled steel tube flanges. *Adv. Civ. Eng.* 2022 (4), 1–24. doi:10.1155/2022/1546263

Ji, J. (2008). "Research on seismic performance and design method of jacketing steel reinforced concrete frame prestressed with bonded tendons,". Doctoral dissertation (Harbin, China: Harbin Institute of Technology).

Ji, J., Yu, D. Y., Jiang, L. Q., Liu, Y. C., Yang, M. M., Song, H. Y., et al. (2020). Research on axial compression bearing capacity of different-strength concrete filled double steel tube short columns. *Build. Struct.* 50 (5), 120–129. doi:10.19701/j.Jzjg.2020.05.021

Ji, J., Zeng, W., Jiang, L., He, L., Ren, H., Chai, Q., et al. (2021b). Hysteretic behavior on asymmetrical composite joints with concrete-filled steel tube columns and unequal high steel beams. *Symmetry* 13, 2381. doi:10.3390/sym13122381

Ji, J., Zheng, W. Z., and Zhang, W. F. (2011). Parameter analysis on dynamic performance of prestressed H-steel reinforced concrete composite beams. *Jianzhu Kexue Yu Gongcheng Xuebao(Journal Archit. Civ. Eng.* 28 (1), 33–41. doi:10.19815/j.jace.2011.01.007

Jia, J. Q., Li, M. M., and Cai, J. (2013a). Experimental investigation on shear bearing capacity of prestressed steel reinforced ultra-high-strength concrete beams. *Build. Struct.*

Jia, J. Q., Yao, D. L., and Yu, F. (2013b). Experimental study on shear performance of prestressed steel ultra-high reinforced concrete beam under concentrated load. *J. Build. Struct.* 34 (12), 112–120. doi:10.6052/j.issn.1000-4750.2013.03.0155

Jiang, Q., Wang, H., Chong, X., Feng, Y., and Ye, X. (2021). Flexural behavior of high-strength, steel-reinforced, and prestressed concrete beams. *Front. Struct. Civ. Eng. Engl. Version* 15 (1), 227–243. doi:10.1007/s11709-020-0687-3

Kuntal, V. S., Chellapandian, M., and Prakash, S. S. (2017). Efficient near surface mounted cfrp shear strengthening of high strength prestressed concrete beams – An experimental study. *Compos. Struct.* 180, 16–28. doi:10.1016/j.compstruct.2017.07.095

Teng, L. L. G. (2003). Design-oriented stress–strain model for frp-confined concrete. *Constr. Build. Mater*. doi:10.1016/s0950-0618(03)00045-x

Lu, X. R., Meng, G., and Gao, J. C. (2021). Experimental study on fatigue performance of partially prestressed steel reinforced ultra-high strength concrete precast beams. *Archit. Ski.* 27 (1), 201–204. doi:10.19953/j.at.2021.s1.045

Li, F. (2007). "Experimental research on the carrying capacity of the prestressed steel reinforced concrete beam,". Doctoral dissertation (Chongqing, China: ChongQing University).

Meng, G., Jinqing, J., Juncheng, Gao., and Hao, Y. (2014). Experiment and calculation of crack width of prestressed steel-reinforced ultra-high strength concrete beams. *J. South China Univ. Technology:Science Ed.* 42 (10), 9. doi:10.3969/j.issn.1000-565X.2014.10.017

Park, R. (1989). Evaluation of ductility of structures and structural assemblages from laboratory testing. *Bull. N. Z. Natl. Soc. Earthq. Eng.* 22, 155–166. doi:10.5459/bnzsee.22.3.155-166

Qian, J., Cheng, L., and Zhou, D. (2002). Behavior of axially loaded concrete columns confined with ordinary hoops. *Qinghua Daxue Xuebao/journal Tsinghua Univ.* 42 (10), 1369–1373. doi:10.1007/s11769-002-0073-1

Steinberg, E. (2010). Structural reliability of prestressed uhpc flexure models for bridge girders. *J. Bridge Eng.* 15 (1), 65–72. doi:10.1061/(ASCE)BE.1943-5592.0000039

Sun, J. Y., Li, G. P., and Fan, L. C. (2006). Experimental study on the tension and moment capacities of the prestressed steel reinforced concrete beams. *J. Tongji Univ. Sci.* 34 (1), 17–21. doi:10.1016/S1010-5182(06)60391-0

Taylor, C. W., Montoya, K. F., Jáuregui, David V., Newtson, C. M., and Weldon, B. D. (2011). Feasibility analysis of using UHPC in prestressed bridge girders. *Struct. Congr.*, 203–214. doi:10.1061/41171(401)19

Wang, H., Marino, E. M., Pan, P., Liu, H., and Nie, X. (2018). Experimental study of a novel precast prestressed reinforced concrete beam-to-column joint. *Eng. Struct.* 156, 68–81. doi:10.1016/j.engstruct.2017.11.011

Wang, J. B., Jia, J. Q., and Meng, G. (2012). Non-linear analysis of prestressed steel-reinforced ultra-high-strength concrete beam subjected to bending. *J. Water Resour. Archit. Eng.*

Wang, J., Wu, D., Zheng, W. Z., Clarkson, W. A., and Ibsen, M. (2009). Single frequency Tm-doped fibre DBR laser at 1943 nm. *J. Harbin Inst. Technol.* 41 (6), 22–27. doi:10.1109/CLEOE-EQEC.2009.5194697

Wu, P., Guo, Y., Zhu, D., Jin, W., and Liang, R. (2019). Flexural performances of prestressed high strength concrete piles reinforced with hybrid gfrp and steel bars. *Mar. Georesources Geotechnol.* 38 (5), 518–526. doi:10.1080/1064119X.2019.1600081

Xue, W. C., Yang, F., Su, X. L., and Lu, P. (2007). Experimental studies on prestressed steel reinforced concrete beams under low reversed cyclic loading. *J. Harbin Inst. Technol.* 39 (8), 1185–1190. doi:10.1002/cem.1038

Yao, D., Jia, J., Wu, F., and Yu, F. (2014). Shear performance of prestressed ultra high strength concrete encased steel beams. *Constr. Build. Mater.* 52, 194–201. doi:10.1016/j.conbuildmat.2013.11.006

Yu, Z., and Ding, F. (2003). Unified calculation method of compressive mechanical properties of concrete. *J. Build. Struct.*

Zhao, H. T. (2001). Steel-concrete composite structure. *Science Press*.

Zhao, J. D., Liu, L. X., Qiu, H. X., Zhu, A. P., Wang., X. F., and Ke, C. H. (2015). Design Code for concrete structure (gb 50010-2010). *Constr. Technol.* (10), 3.

Zhou, X. N., Xu, J., and Lian, F. (2009). Non-linear analysis of prestressed steel reinforced concrete beam subject to bending. *J. Shandong Jianzhu Univ.*